



## Application of Omega vortex identification method in cavity buffeting noise<sup>\*</sup>

Yang-hui Zhang, Xing-jun Hu, Wei Lan, Yi-chen Liu, Mo Wang, Jing-yu Wang

*State Key Laboratory of Automobile Simulation and Control, Jilin University, Changchun 130025, China*

(Received December 19, 2019, Revised March 26, 2020, Accepted April 12, 2020, Published online April 28, 2021)  
 ©China Ship Scientific Research Center 2021

**Abstract:** The cavity buffeting noise is related to the free shear layer oscillation and the periodic vortex shedding, where weak vortices coexist with strong vortices and the strong shear phenomenon also exists at the opening of the cavity. Therefore, it is of great significance to accurately capture vortices at the opening for the control of the cavity buffeting noise. This paper first compares the Omega vortex identification method with the  $\mathcal{Q}$  and  $\lambda_2$  criteria based on the large eddy simulation (LES) of the backward-facing step flow, and it is found that the Omega method enjoys the following advantages: it is not sensitive to a moderate threshold change and  $\mathcal{Q} = 0.52$  can be used as a fixed threshold, it can capture both the strong and weak vortices at the same time; and it will not be contaminated by the shear. Then the Omega ( $\mathcal{Q}$ ) method is applied to the LES of the cavity buffeting noise: the mechanism of the cavity buffeting noise is studied based on a simple cavity model firstly, and then the effects of the incoming boundary layer thicknesses and the incoming boundary layer shapes on the cavity buffeting noise are analyzed. The results show that: the  $\mathcal{Q}$  method clearly captures the processes of the vortex generation, development, collision and fragmentation, verifying that the generation of the cavity buffeting noise is related to the free shear layer oscillation and the periodic vortex shedding; as the thickness of the incoming boundary layer increases, the free shear layer becomes more stable and the Helmholtz resonance is avoided effectively, thereby the cavity buffeting noise is reduced effectively, adding a convexity upstream of the cavity opening to interfere the shape of the incoming boundary layer to reduce the acoustic feedback effect can reduce the cavity buffeting noise effectively.

**Key words:** Vortex identification, Omega ( $\mathcal{Q}$ ), buffeting noise, boundary layer

### Introduction

While bringing convenience to people, the automobiles also bring about a series of negative effects, among which, the aerodynamic noise pollution seriously affects the comfort of drivers and passengers. In a survey of automotive quality, about 50% of the customer complaints on wind noise relate to buffeting<sup>[1]</sup>. The buffeting is a wind noise of a low frequency (< 20 Hz), but in a high level (> 100 dB), to be perceived inside a moving automobile at a certain speed, if a side window or sunroof is open. The buffeting noise with characteristics of low frequency and high intensity may make the passenger tired and irritable, thus affect the vehicle ride comfort and driving safety<sup>[2]</sup>.

Early studies show that the mechanisms of

inducing buffeting noise include<sup>[3-5]</sup>: (1) The feedback mechanism: due to the instability of the shear layer, the vortex shedding is induced at the leading edge of the cavity, and the vortex moves downstream and hits the trailing edge of the cavity, generating pressure waves and propagating upstream in the form of acoustics, to interfere with the flow at the leading edge and induce a new round of vortex shedding. (2) The acoustic resonance: when the vortex shedding frequency at the opening of the cavity is the same as or close to the natural frequency of the cavity, the Helmholtz resonance will occur with a strong buffeting noise generated.

The studies of related issues started earlier in other countries. In 1981, Nelson et al.<sup>[6]</sup> expounded the cavity resonance mechanism from the perspective of fluid energy and momentum exchange by means of experiments. In 1994, Ota et al.<sup>[7]</sup> confirmed the critical velocity of wind-induced vibration and explored the effect of guide plate with different angles on buffeting noise suppression. In 2013, Mendonca<sup>[8]</sup> considered the influence of the elastic, structural damping, leakage and other factors on the simulation of buffeting noise. In 2019, Dunai et al.<sup>[9]</sup> evaluated the buffeting noise of passenger vehicle BMV530d in

\* Projects supported by the Natural Nature Science Foundation of China (Grant No. 51875238).

**Biography:** Yang-hui Zhang (1994-), Male, Ph. D. Candidate, E-mail: 1950175242@qq.com

**Corresponding author:** Jing-yu Wang, E-mail: wangjy@jlu.edu.cn

real measurement conditions in an outdoors highway at different speeds. Compared with other countries, the researches of the buffeting noise started later in China. In 2007, Gu et al.<sup>[10]</sup> of Hunan University reviewed the mechanisms and the control methods for the buffeting noise. In 2010, Wang et al.<sup>[11]</sup> simulated the transient flow field outside the car to study the characteristics of the sunroof buffeting noise, and suppressed it by installing a deflector and opening the sunroof reasonably. In 2012, Wang et al.<sup>[12]</sup> studied the characteristics of the side window buffeting noise of a car, and obtained the relationship between the speed, the interior volume, the opening position, the number of side opening windows and the frequency and the intensity of the buffeting noise, and proposed two kinds of noise reduction measures.

Since the buffeting noise is mainly related to the vortex shedding caused by the instability of the shear layer at the cavity opening, it is of great significance to study the development of the boundary layer and the oscillation characteristics of the shear layer in understanding the mechanism of the buffeting noise. Wang<sup>[4]</sup> discussed the causes of the buffeting noise based on a simple cavity model, and showed that the simulation data is in good consistency with the experiment, without involving the influence of the boundary layer development of the incoming flow on the cavity buffeting noise. Liu et al.<sup>[13]</sup> studied the effect of the turbulent boundary layer thickness on the three-dimensional cavity flow of a high Mach number, but with the vehicle always at low Mach number, so the aerodynamic characteristics would be different. Other studies of the cavity flow at home and abroad mainly focus on the influence of the Mach number, the aspect ratio and other parameters on the cavity buffeting noise, but not so much on the boundary layer of the incoming flow.

In this paper, the computational fluid dynamics software Fluent and the  $\Omega$  vortex identification method are used to study the mechanism of the cavity buffeting noise based on a simple cavity model and the influence of the incoming boundary layer thickness and shape on the cavity buffeting noise.

## 1. Review of vortex identification methods

The vortex identification methods can be divided into three generations. The first generation is the vorticity-based vortex identification method, but with the vorticity, the real rotation region cannot be distinguished from the shear layer region, so a vortex cannot be adequately described by the vorticity<sup>[14]</sup>. The second generation is based on the eigenvalue of the velocity gradient tensor  $\nabla V$ , and two representative criteria is the  $Q$  criterion and the  $\lambda_2$  criterion. The  $Q$  criterion is introduced by Hunt et al.<sup>[15]</sup>, with

$Q$  defined as

$$Q = \frac{1}{2} (\|B\|_F^2 - \|A\|_F^2) \quad (1)$$

where  $A$ ,  $B$  are the symmetric and antisymmetric parts of  $\nabla V$ . The  $\lambda_2$  criterion is introduced by Jeong and Hussain<sup>[16]</sup>, with  $\lambda_2$  being the second eigenvalue of the symmetric tensor  $A^2 + B^2$ . With these eigenvalue-based criteria, user-specified thresholds are required and different thresholds will produce different vortex structures<sup>[14]</sup>.

To overcome these weaknesses, Liu et al.<sup>[17]</sup> proposed a new generation of vortex identification methods: the Omega ( $\Omega$ ) vortex identification method in 2016, with  $\Omega$  defined as a ratio of the vorticity tensor norm squared over the sum of the vorticity tensor norm squared and the deformation tensor norm squared, expressed as

$$\Omega = \frac{\|B\|_F^2}{\|A\|_F^2 + \|B\|_F^2 + \varepsilon} \quad (2)$$

where  $\varepsilon$  is a small positive parameter to avoid non-physical noises. The  $\Omega$  method was later modified by Dong et al.<sup>[18]</sup>, with  $\varepsilon$  defined as

$$\varepsilon = 0.001 \times (b - a)_{\max} \quad (3)$$

where  $a = \|A\|_F^2$ ,  $b = \|B\|_F^2$ . In this way, the manual adjustment of  $\varepsilon$  in many cases can be avoided.  $\Omega = 0.51$  or  $\Omega = 0.52$  can be used as the fixed threshold to capture both strong and weak vortex structures at the same time, for the  $\Omega$  method is very insensitive to a moderate threshold change<sup>[14]</sup>. Liu et al.<sup>[19]</sup> proved that the  $\Omega$  method is Galilean invariant under the transformations of a spatial static rotation and a constant-velocity translation.

And then to extract the rigid rotation part from the fluid motion, a new vortex vector "Liutex/Rortex" and its exact form and mathematical definition were defined by Liu et al.<sup>[20]</sup>, Gao and Liu<sup>[21]</sup>, to clearly represent both the direction and the magnitude of the rotational motion. Wang et al.<sup>[22]</sup> derived an explicit formula to calculate the magnitude of the Liutex vector as

$$R = \sqrt{\langle \omega, r \rangle^2 - 4\lambda_{ci}^2} \quad (4)$$

where  $\omega$  is the vorticity vector,  $r$  is the local rotational axis. Wang et al.<sup>[23]</sup> proved that Rortex is invariant under the Galilean transformation. Gao et al.<sup>[24]</sup> defined the vortex core center as a line where the Liutex magnitude gradient vector is aligned with

the Liutex vector. Dong et al.<sup>[25]</sup> first combined the Liutex core line method with the snapshot proper orthogonal decomposition to analyse the vertical structures in MVG wake. Charkrit et al.<sup>[26]</sup> analysed the hairpin vortex formation in natural flow transition based on the new method of the vortex core line also known as Liutex core line and proper orthogonal decomposition.

Recently, Dong et al.<sup>[27]</sup> proposed a new method named Omega-Liutex ( $\Omega_R$ ) which combines the  $\Omega$  and Liutex/Rortex methods, with  $\Omega_R$  expressed as

$$\Omega_R = \frac{\beta^2}{\alpha^2 + \beta^2 + \varepsilon} \quad (5)$$

where

$$\alpha = \frac{1}{2} \sqrt{\left( \frac{\partial V}{\partial Y} - \frac{\partial U}{\partial X} \right)^2 + \left( \frac{\partial V}{\partial X} + \frac{\partial U}{\partial Y} \right)^2},$$

$$\beta = \frac{1}{2} \left( \frac{\partial V}{\partial X} - \frac{\partial U}{\partial Y} \right)$$

and  $\varepsilon$  is similarly defined as follows

$$\varepsilon = b \times (\beta^2 - \alpha^2)_{\max} \quad (6)$$

where  $b$  is a small fixed positive number, e.g., 0.001.  $\Omega_R$  can be always set as 0.52 to capture vortex structures in different cases and at different timesteps<sup>[27]</sup>.

## 2. Verification of the simulation methods

### 2.1 Comparison of vortex identification methods

The backward-facing step flow with the boundary layer separation and reattachment is a common complicated flow phenomenon in engineering, including the generation, the development and the dissipation of vortices<sup>[28]</sup>. This part compares the  $\Omega$ ,  $\lambda_2$  criteria and the  $\Omega$  method in the sensitivity to the threshold change and the ability to capture both strong and weak vortices based on the LES for the backward-facing step flow.

The size and the mesh of the backward-facing step are shown in Fig. 1. The step height  $H = 0.038$  m, and the width (in  $Y$  direction) =  $2H$ . The origin of the coordinate system is located at the beginning of the wall under the step of the longitudinal symmetry plane. The thickness of the first layer of the boundary layer is 0.02mm, with a total of 17 layers and a growth rate of 1.2. For the volume grid, the hexahedral structure grid is adopted, and the total number of grids is  $2.99 \times 10^6$ . The reference experimental data are from Ref. [29].



Fig. 1 The size and mesh of the backward-facing step

The boundary conditions: the inlet type is the velocity-inlet,  $U_{ref} = 11.3$  m/s, and the boundary layer thickness at the inlet is 40.5mm according to the 1/7 power law<sup>[13]</sup>, which is consistent with the experiment, the outlet type is the pressure-outlet (101 325 Pa), the ground is a no slip wall; the rest are symmetrical walls.

In this case, the realizable  $k - \varepsilon$  turbulence model is used for the steady simulation before the transient simulation to provide the initial value for the transient simulation, so as to improve the accuracy and the convergence of the simulation. For the transient simulation, the wall modeled LES (WMLES) subgrid scale model is used, and the time step  $\Delta t = 0.002$  s.

The simulation method is verified by comparing the location of the reattachment point on the longitudinal symmetry surface and the time-averaged velocity profile. The reattachment point is the point where the wall shear stress  $\tau_w$  is equal to 0 again<sup>[30]</sup>. As shown in Table 1, the location of the simulation reattachment point is very close to that of the experiment with an error of only 0.47%. It can be seen from Fig. 2 that the mean velocity profiles of the LES at the five monitoring lines are in good agreement with those of the experiment. The above results show that the simulation method is accurate enough.

**Table 1 Location of reattachment point**

Location $x / m$	Experiment	LES	Error
0.2572	0.256	0.256	0.47%

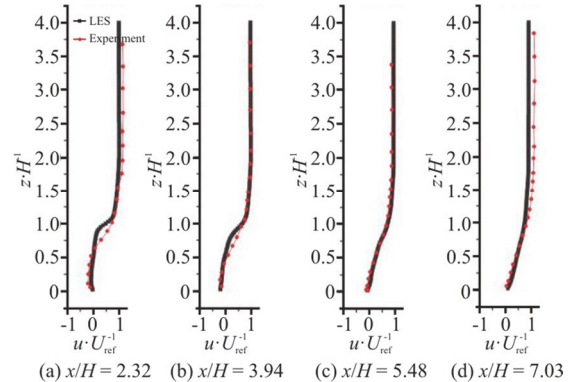


Fig. 2 (Color online) Time-averaged streamwise velocity profiles

Due to the strong shear in the backward-facing step flow, the vorticity-based vortex identification method cannot capture the effective vortex structure. Figures 3–5 show the vortex structures captured by the  $Q$ ,  $\lambda_2$  criteria and the  $\Omega$  method with different thresholds at  $t = 0.14$  s. When the flow just separates at the back edge of the step (inside the black oval line), the vortex structures identified by  $Q$  with different thresholds are completely different, very sensitive to the change of the threshold and seriously contaminated by the shear (Fig. 3). When  $Q = 2\,000$ , the weak vortex structures cannot be captured because of the seriously contamination; when  $Q = 60\,000$ , the shear contamination is attenuated and some weak vortices can be captured; when  $Q = 10\,000$ , the shear contamination becomes very small, but because the threshold is too large, some weak vortices disappear. Similarly, almost the same result occurs when the threshold of  $\lambda_2$  ranges from  $-1\,000$  to  $-10\,000$  (Fig. 4). In contrast, the  $\Omega$  method is not sensitive to a moderate threshold change and is not contaminated by the shear (Fig. 5). When the threshold of  $\Omega$  is 0.52, 0.55 and 0.58, the vortex structures identified are very similar, and the strong and weak vortices can be captured at the same time, which is one of the obvious advantages of the  $\Omega$  method.

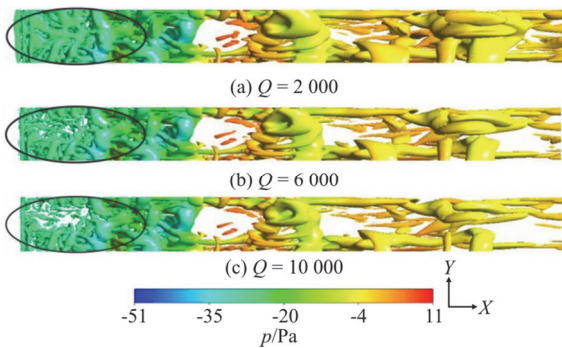


Fig. 3 (Color online)  $Q$  iso-surfaces

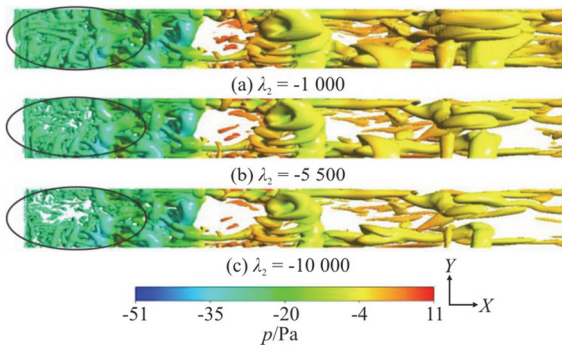


Fig. 4 (Color online)  $\lambda_2$  iso-surfaces

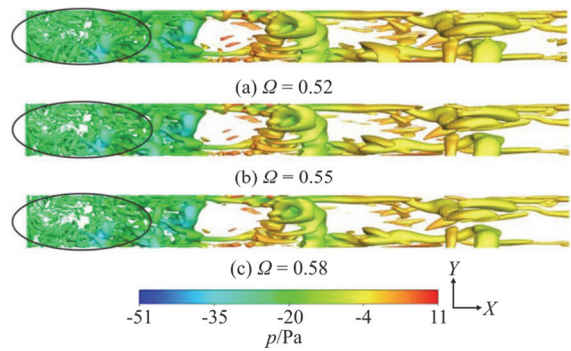


Fig. 5 (Color online)  $\Omega$  iso-surfaces

Figure 6 shows the  $\Omega = 0.52$  iso-surfaces at four different moments. As shown in the figure, the  $\Omega$  method can capture both strong and weak vortices clearly, without shear contamination. The  $\Omega$  method clearly captures the generation and development processes of the vortex in the backward-facing step flow, and it is seen that the vortex in the black oval line grows gradually and moves backwards. From what has been discussed above, the  $\Omega$  method has three obvious advantages over the  $Q$  and  $\lambda_2$  criteria: the  $\Omega$  method is not sensitive to a moderate threshold change and  $\Omega = 0.52$  can be used as a fixed threshold, the  $\Omega$  method can capture strong vortices and weak vortices at the same time, the  $\Omega$  method will not be contaminated by the shear.

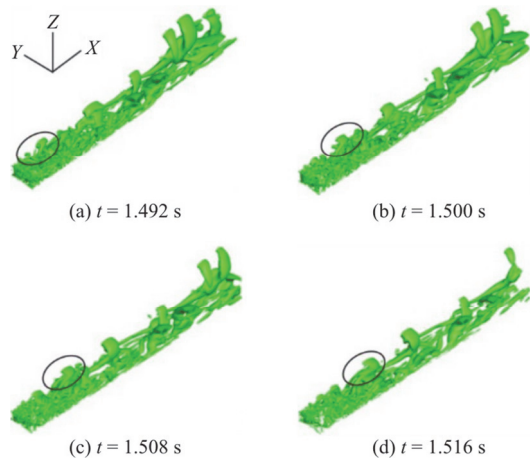


Fig. 6 (Color online) Iso-surfaces of  $\Omega = 0.52$

## 2.2 Simple cavity buffeting noise research

### 2.2.1 Simple cavity model

The simple cavity model is built according to Ref. [4], as shown in Fig. 7. The opening is located in the center of the top surface of the cavity, and the monitoring point is located in the center of the bottom

of the cavity. The origin of the coordinate system is located at the center of the upper surface of the cavity opening. The sizes of the computational domain are shown in Fig. 8. The leading edge of the cavity opening is 0.40 m from the inlet, and the width of the computational domain is 0.53 m. The thickness of the first layer of the boundary layer is 0.05 mm, with a total of 12 layers and a growth rate of 1.2. For the volume grid, the hexahedral structure grid is adopted. Twenty-one monitoring points are set on the longitudinal symmetric surface at the bottom of the cavity to verify the grid independence by comparing the pressure coefficient ( $C_p$ ) at the monitoring points, as shown in Fig. 9, where  $d$  is the distance between the monitoring point and the leading edge at the bottom of the cavity, and  $D$  is the length the cavity along the direction of the flow. When the number of grids reaches  $4.05 \times 10^6$ , the distribution trend of  $C_p$  at the bottom of the cavity remains basically unchanged. Therefore, this grid scheme is selected for the subsequent simulation, as shown in Fig. 8.

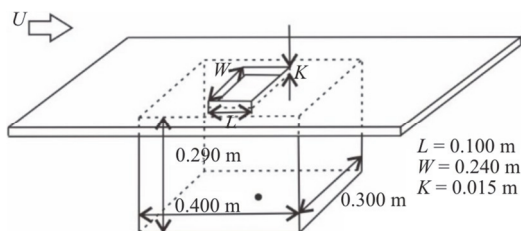


Fig. 7 Simple cavity model

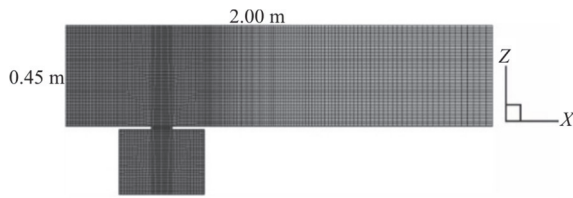


Fig. 8 The size and the mesh of the computational domain

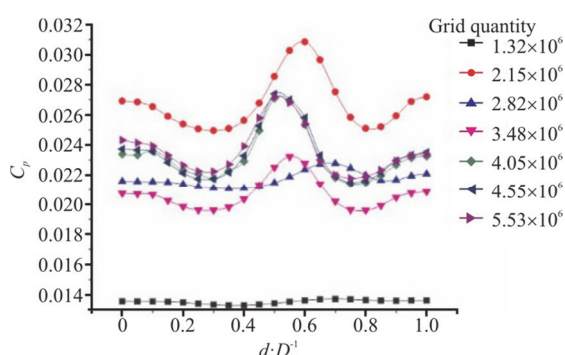


Fig. 9 (Color online) Distribution of  $C_p$  at the bottom of cavity

### 2.2.2 Computational aeroacoustic method

The computational aeroacoustic method is used to calculate the aerodynamic noise directly, that is, to directly extract the acoustic information from the calculation results. The basic idea of the computational aeroacoustic is that the Navier-Stokes equation is used to describe the fluid flow and the sound propagation at the sound source, so the transient Navier-Stokes equation is solved to calculate the generation and propagation processes of the sound. When the computational aeroacoustic method is used to solve the flow field, the sound source and receiver are both in the calculation domain. As long as the monitoring point is specified and the corresponding pressure pulsation information is recorded, the sound data can be directly obtained without using other acoustic models. In this paper, the computational aeroacoustic method is used to accurately determine the cavity buffeting noise. The sound pressure level (SPL) can be expressed as<sup>[31]</sup>

$$\text{SPL} = 20 \times \lg \left( \frac{p'}{p_0} \right) \quad (7)$$

where  $p'$  is the pulsating pressure,  $p_0$  is the reference pressure,  $2 \times 10^{-5}$  Pa.

### 2.2.3 LES method

The boundary conditions: the inlet type is the velocity-inlet,  $U_{\text{ref}} = 25.0$  m/s, the turbulence intensity is 0.5% and the hydraulic diameter is 0.034 m, the outlet is the pressure-outlet (101 325 Pa), the ground and the cavity are no slip walls; the rest are symmetrical walls. The material is ideal gas.

Similar to the back-step flow simulation, the realizable  $k - \varepsilon$  turbulence model is also used for the steady simulation before the transient simulation. The SIMPLE pressure-velocity coupling method and the second order upwind discretization scheme are used in the simulation and the time step  $\Delta t = 0.001$  s.

In the subgrid scale model of the LES, the DSM (Dynamic Smagorinsky-Lilly Model), the wall-adapting local eddy-viscosity model (WALEM) and the wall modeled LES (WMLES) are adopted, respectively, and the results are compared with the experimental data in Ref. [4]. The results of the WMLES are closer to the experimental data, so this model is used for the subsequent research (Table 2).

**Table 2** The comparison of different subgrid scale models with experiment

Subgrid scale model	SPL peak/dB	Frequency /Hz
DSLM	131.81	103.90
WALEM	131.05	104.02
WMLES	129.01	104.81
Experiment	123.00	103.00

### 2.2.4 Analysis of WMLES simulation results

The pressure cloud diagrams of a period  $T$  on the longitudinal symmetric surface are shown in Fig. 10. At  $t = 0$ , the vortices begin to shed at the leading edge of the cavity opening. From  $t = T/5$  to  $t = 2T/5$ , the low-pressure vortex moves downstream, and with the invasion of the high pressure outside, the pressure inside the cavity rises to the highest. At  $t = 3T/5$ , the vortex begins to hit the rear edge of the cavity opening, and the broken low-pressure vortex invades the cavity, reducing the pressure inside the cavity. At  $t = 4T/5$ , the vortex is completely broken and the pressure inside the cavity reaches the minimum. At time  $t = T$ , a new vortex is induced at the leading edge and a new cycle begins. One sees a periodic pressure pulsation in the cavity with the generation, the shedding, the development and the breakage of the vortex at the opening, which is caused by the self-excited oscillation in the cavity caused by the feedback mechanism.

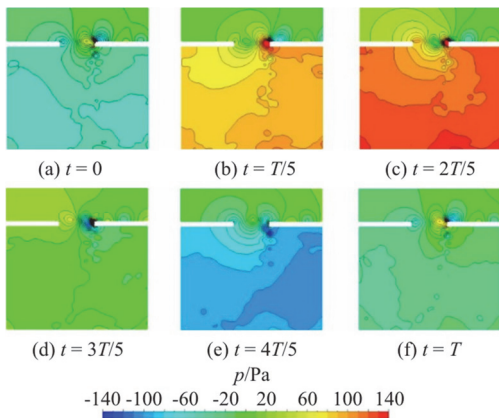


Fig. 10 (Color online) Pressure cloud diagrams

The  $\Omega$  cloud diagrams of a period  $T$  on the longitudinal symmetric surface are shown in Fig. 11. The region of  $\Omega \geq 0.52$  can be considered as the vortex region, and the larger the value of  $\Omega$  is, the closer the region is to the vortex core. Compared with the pressure cloud diagram, from the  $\Omega$  cloud diagram, one can observe the weak vortices invading the cavity in addition to the strong vortices at the opening of the cavity on the one hand, which further demonstrates the advantage of the  $\Omega$  method in capturing both strong and weak vortices, on the other hand, the shape of the vortex region is clearer and more intuitive. The  $\Omega$  cloud diagrams with iso-surfaces of  $\Omega = 0.52$  of a period  $T$  on the longitudinal symmetric surface are shown in Fig. 12. From Figs. 11 and 12, we can clearly observe the processes of the vortex generation, shedding, development and breakage.

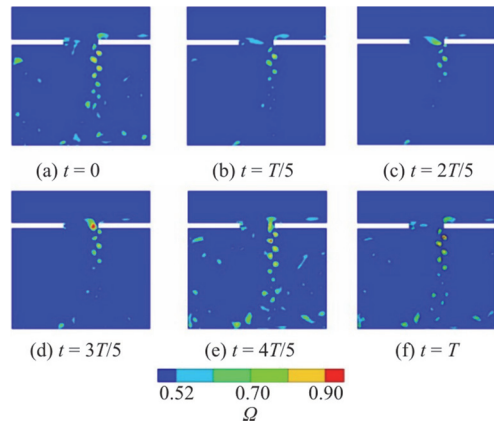


Fig. 11 (Color online)  $\Omega$  cloud diagrams

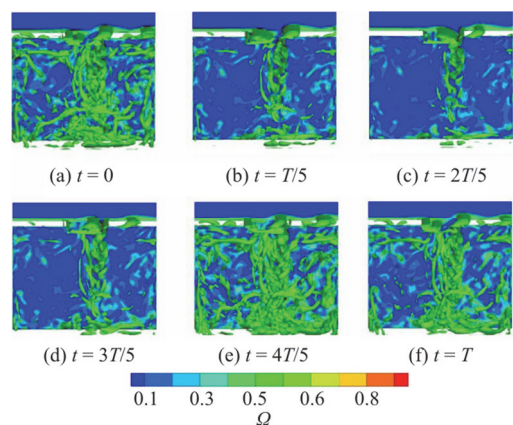


Fig. 12 (Color online)  $\Omega$  cloud diagrams with iso-surfaces of  $\Omega = 0.52$

21 monitoring lines are established at the opening of the cavity, and 29 monitoring points are arranged on each line, as shown in Fig. 13. The turbulence eddy dissipation (TED) and the turbulence kinetic energy (TKE) can be used to characterize the pulsation energy in the flow field. It can be seen from Figs. 14 and 15 that, the closer the location to the rear edge of the cavity opening, the greater the TKE and the TED at that location will be, due to the violent oscillation of the shear layer near the rear edge caused by the impact and the breakage of the vortex.

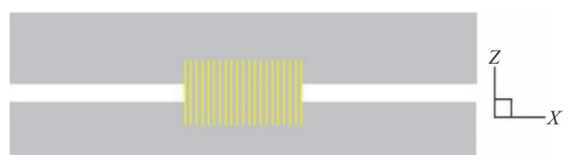


Fig. 13 (Color online) Distribution of monitoring points at cavity opening

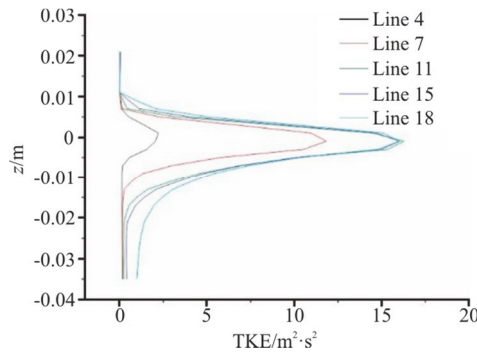


Fig. 14 (Color online) Distribution of TKE

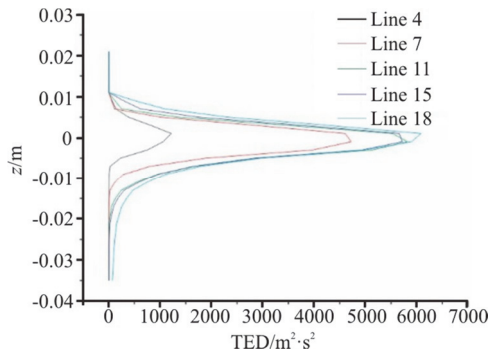


Fig. 15 (Color online) Distribution of TED

The empirical formula of the natural frequency of the cavity is

$$f = \frac{c}{2\pi} \sqrt{\frac{A}{VM}} \quad (8)$$

where  $c$  is the sound velocity,  $A$  is the area of the cavity opening,  $V$  is the volume of the cavity,  $M = K + 0.96\sqrt{A}$  and  $K$  is the thickness of the cavity opening. According to formula (8), the natural frequency of the simple cavity model is about 110 Hz.

The SPL spectrum diagrams at different velocities  $U$  are shown in Fig. 16. When  $U = 50$  km/h, there is no obvious resonance detected on the SPL spectrum diagram and the quasi-resonance begins when  $U = 70$  km/h. As can be seen from Table 3, when  $U = 90$  km/h and  $U = 110$  km/h, the buffeting frequencies are around 110 Hz, and the SPL peak reaches 129 dB. Thus, when the frequency of the buffeting noise is close to the natural frequency of the cavity, the Helmholtz resonance will occur inside the cavity. The closer the frequency of the buffeting is to the natural frequency, the stronger the resonance intensity is, and the higher the SPL of the buffeting noise will be.

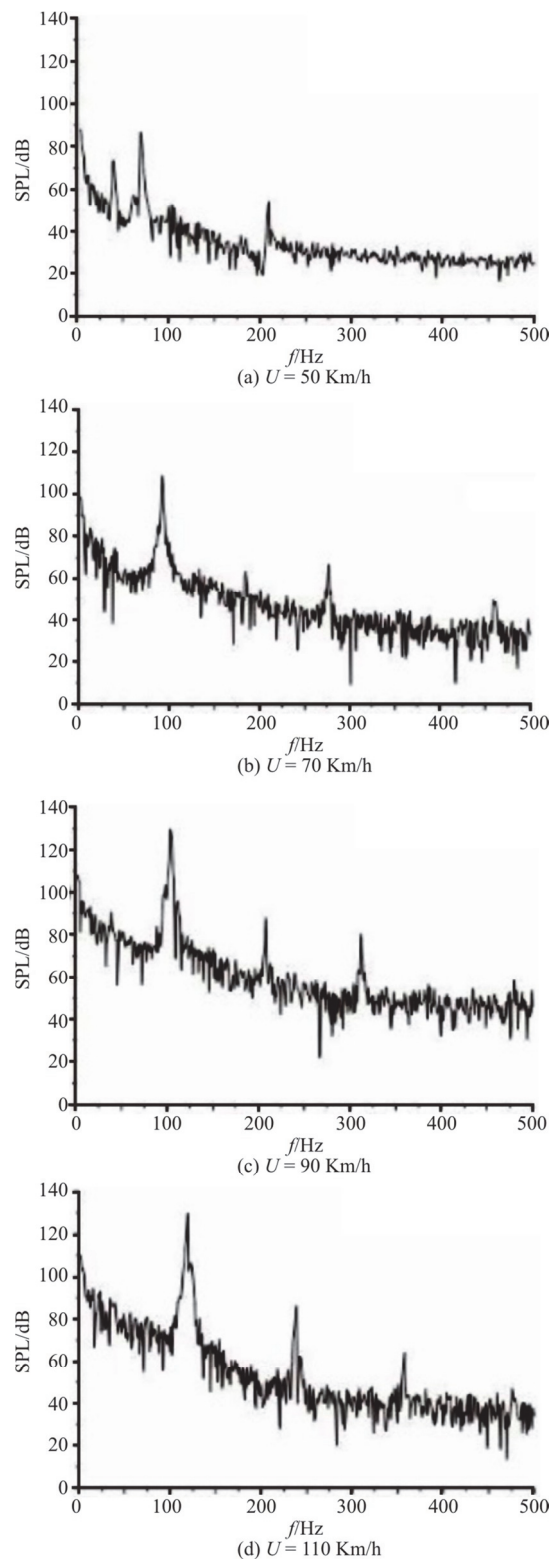


Fig. 16 SPL spectrum diagram

### 3. The influence of thickness of incoming boundary layer

The influence of the inlet boundary layer thickness on the cavity buffeting noise is studied in

this section by considering the inlet boundary layer thickness of 0 mm, 8 mm, 16 mm, 24 mm, 32 mm and 40 mm, respectively according to the 1/7 power law<sup>[13]</sup>. The SPL peaks and frequencies for different inlet boundary layer thicknesses are shown in Table 4. With the increase of the inlet boundary layer thickness, the buffeting frequency gradually decreases, being far away from the natural frequency (110 Hz), and the SPL peak at the monitoring point gradually decreases, which indicates that increasing the boundary layer thickness of the incoming flow can effectively avoid the Helmholtz resonance, thus reducing the effect of the buffeting noise.

**Table 3 SPL peak and frequency**

Velocity/km·h <sup>-1</sup>	SPL peak/dB	Frequency/Hz
70	108.71	91.92
90	129.01	104.81
110	129.63	119.19

**Table 4 SPL peak and frequency**

Thickness/mm	SPL peak/dB	Frequency/Hz
0	129.01	104.81
8	127.13	104.90
16	126.79	102.02
24	125.78	100.00
32	123.40	97.98
40	119.65	95.96

The stability of the free shear layer can be evaluated by the disturbance intensity development, i.e., the distribution of the maximum RMS value of the streamwise velocity fluctuation on the monitoring lines, as shown in Fig. 17, where  $l$  is the distance between the monitoring line and the leading edge of the cavity opening and  $L$  is the length of the cavity opening along the flow direction. From the leading edge to the midpoint of the cavity opening, the disturbance intensity increases approximately linearly. As the thickness increases, the growth rate of the disturbance intensity decreases, the stability of the free shear layer increases and the amplitude of the oscillation decreases. Figure 18 shows the streamwise velocity profiles in the cases of different thicknesses. With the increase of the thickness, the curvature of the velocity profile decreases, resulting in a thicker shear layer with a stronger stability.

Figure 19 shows the pressure cloud diagrams within a period  $T$  on the longitudinal symmetric plane when the inlet boundary layer thickness is 8 mm and 40 mm, respectively. Figure 20 shows the pressure cloud diagrams on the longitudinal symmetric plane at  $t = 4T/5$  in cases of different inlet boundary layer thicknesses. With the increase of the boundary layer thickness of the incoming flow, although one can still see the periodic pressure pulsation in the cavity, the pressure of the vortex core gradually increases and the pressure pulsation intensity in the cavity gradually

decreases. When the thickness increases to 40 mm, the pressure pulsation in the cavity is very weak. As can be seen from Figs. 21 and 22, with the increase of the incoming boundary layer thickness, the number of vortices at the cavity opening gradually decreases, and the number of vortices invading in the cavity after colliding with the rear edge gradually reduces, so the low-frequency discrete buffeting noise mainly caused by the large-scale vortex also gradually weakens.

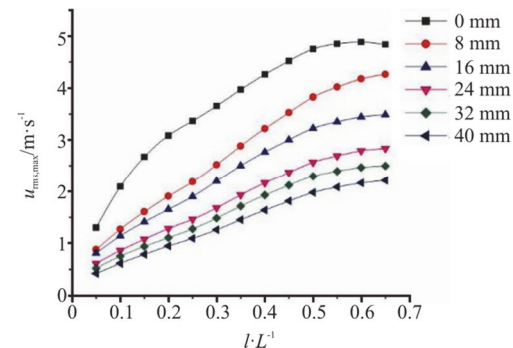


Fig. 17 (Color online) Disturbance intensity development

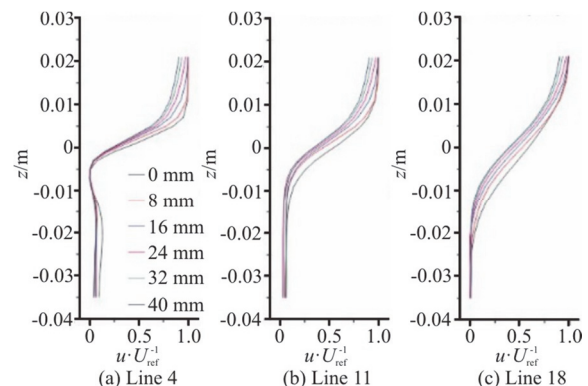


Fig. 18 (Color online) Streamwise velocity profiles

In conclusion, with the increase of the boundary layer thickness of the incoming flow, the vortex shedding frequency at the leading edge becomes far away from the cavity natural frequency gradually, the free shear layer becomes more stable and the amplitude of the oscillation decreases. So the Helmholtz resonance can be avoided and the intensity of the pressure pulsation in the cavity is effectively weakened. Thus the buffeting noise is effectively reduced.

#### 4. The influence of shapes of incoming boundary layer

As shown in Fig. 23, by adding a convexity with a height of 4 mm and 5 mm, respectively, upstream the cavity opening, the shape of the incoming boundary layer is transformed from laminar to turbulent.

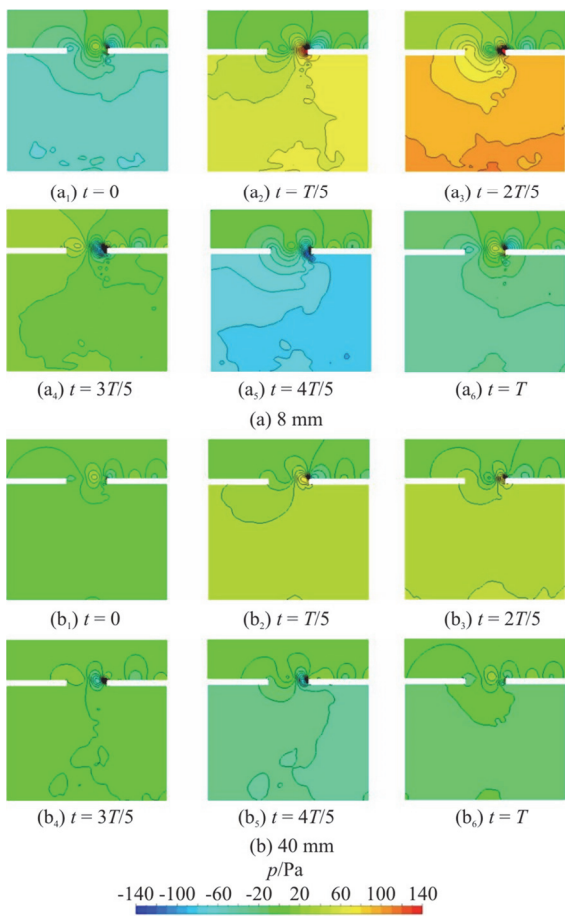


Fig. 19 (Color online) Pressure cloud diagrams

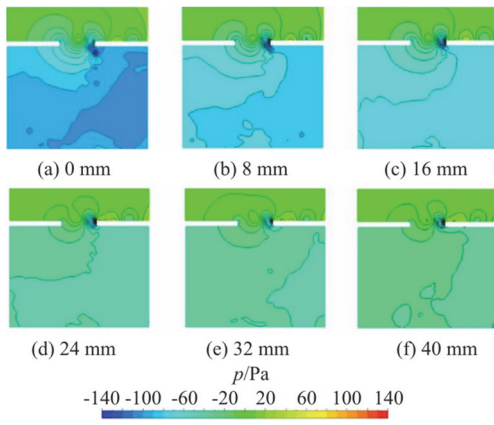
Fig. 20 (Color online) Pressure cloud diagrams at  $t = 4T/5$ 

Figure 24 shows the SPL spectrum diagram at different heights. It can be seen that when a convexity is added upstream the cavity opening, the resonance in the cavity disappears basically. As can be seen from Table 5, with the increase of the height, the buffeting frequency stays about the same and the SPL peak at the monitoring point gradually decreases, which indicates that although the buffeting frequency is close

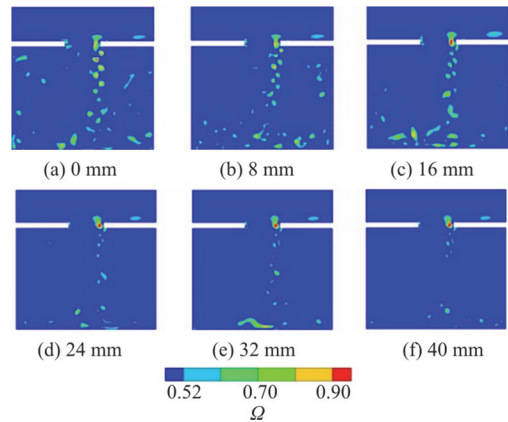
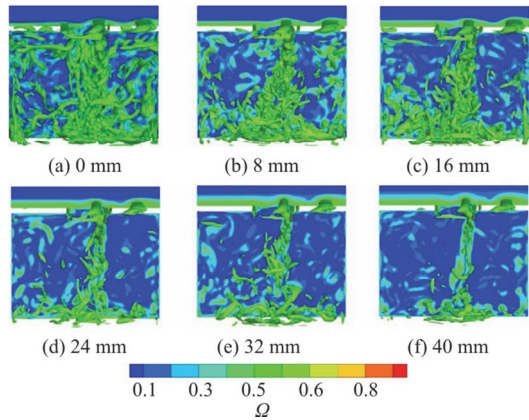
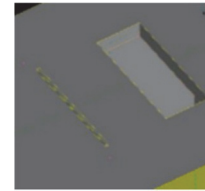
Fig. 21 (Color online) Omega cloud diagrams at  $t = 4T/5$ Fig. 22 (Color online) Omega cloud diagrams with iso-surfaces of  $\Omega = 0.52$  at  $t = 4T/5$ 

Fig. 23 (Color online) The convexity upstream the cavity opening

to the natural frequency of the cavity, adding a convexity can effectively reduce the effect of the acoustic feedback, thus reducing the buffeting noise.

Figure 25 shows the pressure cloud diagrams on the longitudinal symmetric surface within one period T when the height of the convexity is 0 mm and 5 mm, respectively. As can be seen from the figure, when the convexity is added, although one can still see the periodic pressure pulsation inside the cavity, the minimum pressure in the cavity is larger and the maximum pressure is smaller than those in the case of 0mm, so the intensity of the pressure pulsation in the cavity is weakened.

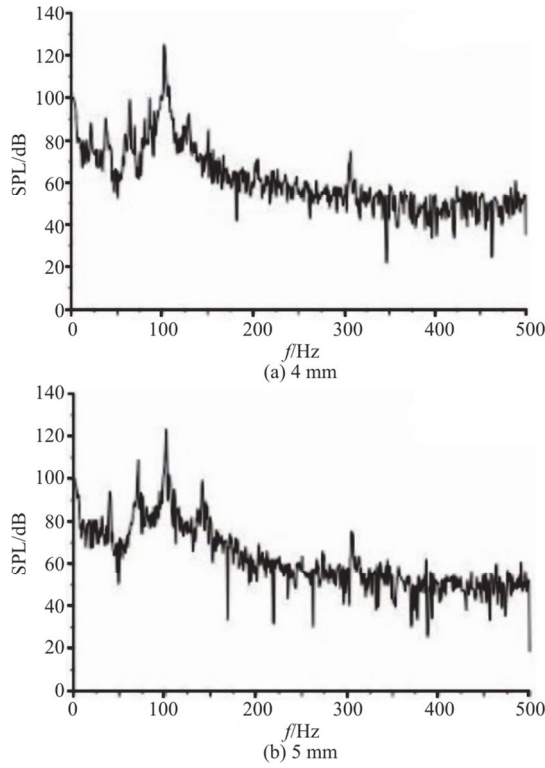


Fig. 24 SPL spectrum diagram

Figures 26 and 27 show the Omega cloud diagrams and the iso-surface of  $\Omega = 0.52$  when the convexity height is 5 mm. As can be seen from the figures, when the convexity is added, both the vortex size at the cavity opening and the vortex intensity decrease, without a significant large vortex motion, and the number of vortices invading the cavity decreases. Therefore, the low frequency discrete buffeting noise mainly caused by the large vortex will also decrease.

Figure 28 shows the development of the disturbance intensity at different heights. When the convexity is added, the disturbance intensity is in a higher level at the leading edge of the cavity, due to the formation of small-scale vortices upstream the cavity opening (as can be seen from Figs. 26 and 27). As shown in Fig. 29, when there is no convexity, the location of the maximum RMS of the streamwise velocity fluctuation is close to the upper surface of the cavity opening, and most of the pulsating energy after the collision between the vortex and the rear edge of the cavity enters the cavity. As the convexity is added, the location of the maximum RMS moves gradually. Figures 30 and 31 show the cloud diagrams of the turbulence kinetic energy and the turbulent eddy dissipation at different heights. These figures show that with adding convexity, the turbulence kinetic energy and the turbulent eddy dissipation are both increase at the cavity opening. But due to the move-

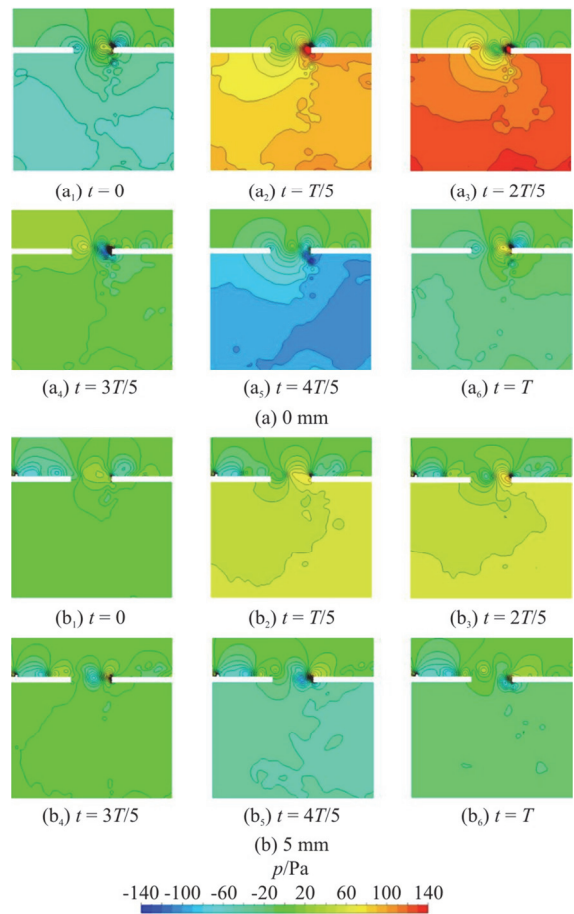
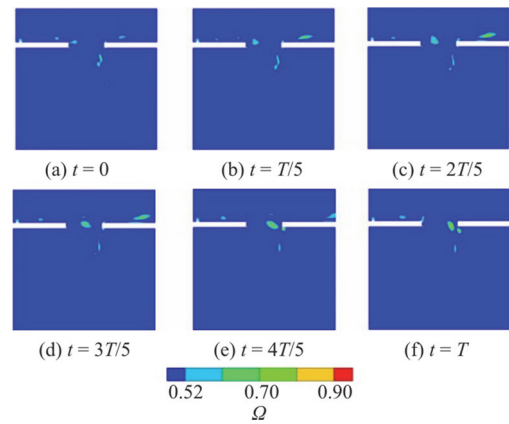


Fig. 25 Pressure cloud diagrams

Fig. 26 (Color online)  $\Omega$  cloud diagrams

ment of the location of the maximum RMS, the shear layer oscillation position moves away from the cavity opening, and the position of the vortices at the cavity opening rises higher (as can be seen by comparing Figs. 11, 12, 26 and 27). Most of the pulsating energy after the collision between the vortex and the rear edge of the cavity propagates backwards instead of entering the cavity, thus reducing the level of the

buffeting noise.

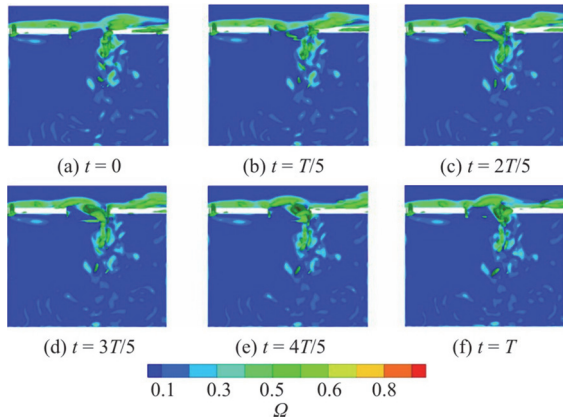


Fig. 27 (Color online)  $\mathcal{Q}$  cloud diagrams with iso-surfaces of  $\mathcal{Q} = 0.52$

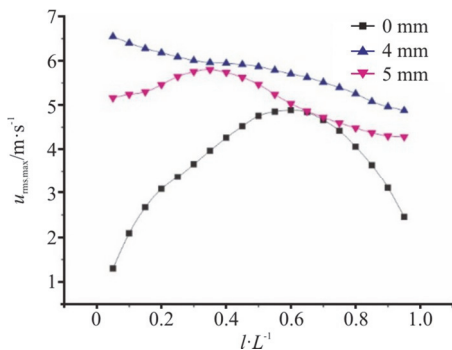


Fig. 28 (Color online) Disturbance intensity development

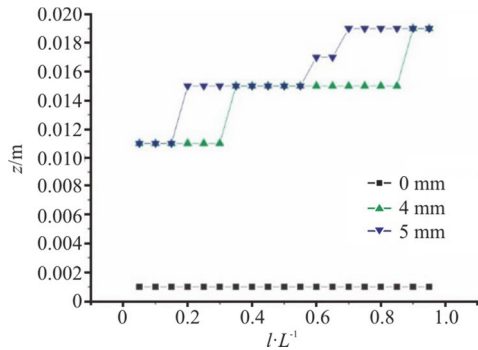


Fig. 29 (Color online) Distribution of the location of the maximum rms of streamwise velocity fluctuation

In conclusion, adding a convexity upstream the cavity opening to interfere the boundary layer shape can effectively reduce the acoustic feedback, thus reducing the buffeting noise. On the one hand, the vortex size at the cavity opening is reduced by adding a convexity, thus reducing the low frequency discrete buffeting noise caused by the large scale vortex. On the other hand, the addition of the convexity makes

the position of the shear layer oscillation far away from the cavity opening, and most of the pulsating energy after the collision between the vortex and the rear edge of the cavity propagates backwards instead of entering the cavity, thus reducing the buffeting noise.

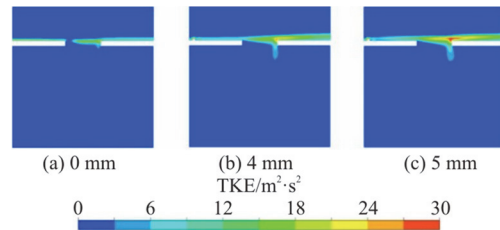


Fig. 30 (Color online) TKE cloud diagrams

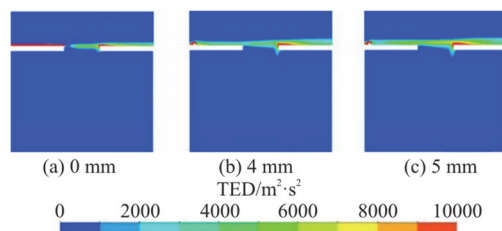


Fig. 31 (Color online) TED cloud diagrams

## 5. Conclusions

The following conclusions are drawn:

(1) This paper compares the  $\mathcal{Q}$  vortex identification method with the  $Q$  and  $\lambda_2$  criteria based on the LES of the backward-facing step flow, and the  $\mathcal{Q}$  method is found to have the following advantages: the  $\mathcal{Q}$  method is not sensitive to a moderate threshold change and  $\mathcal{Q}=0.52$  can be used as a fixed threshold, the  $\mathcal{Q}$  method can capture strong and weak vortices at the same time, the  $\mathcal{Q}$  method will not be contaminated by the shear.

(2) The  $\mathcal{Q}$  method clearly captures the processes of the vortex generation, development, collision and fragmentation, verifying that the generation of the cavity buffeting noise is related to the free shear layer oscillation and the periodic vortex shedding.

(3) With the increase of the boundary layer thickness of the incoming flow, the vortex shedding frequency at the leading edge becomes far away from the cavity natural frequency gradually, the free shear layer becomes more stable and the amplitude of oscillation decreases. So the Helmholtz resonance can be avoided and the intensity of the pressure pulsation in the cavity is effectively weakened. Thus the buffeting noise is effectively reduced.

(4) Adding a convexity upstream the cavity

opening to interfere the boundary layer shape can effectively reduce the effect of the acoustic feedback, thus reducing the buffeting noise. On the one hand, the vortex size at the cavity opening is reduced by adding a convexity, thus reducing the low frequency discrete buffeting noise caused by the large scale vortex. On the other hand, the addition of convexity makes the position of the shear layer oscillation far away from the cavity opening, and most of the pulsating energy after the collision between the vortex and the rear edge of the cavity propagates backwards instead of entering the cavity, thus reducing the buffeting noise.

## References

- [1] An C., Singh K. Sunroof buffeting suppression using a dividing bar [J]. *Tohoku Journal of Experimental Medicine*, 2007, 206(3): 187-194.
- [2] Guo H., Wang Y., Wang X. et al. Study on hybrid LES-LAA method for wind buffeting noise control of vehicle rear windows [J]. *Noise Control Engineering Journal*, 2017, 65(6): 577-589.
- [3] Kook H., Shin S., Cho J. et al. Development of an active deflector system for sunroof buffeting noise control [J]. *Journal of Vibration and Control*, 2014, 20(16): 2521-2529.
- [4] Wang Y. Comprehensive study of generation mechanism and reduction methods of vehicle wind rush noise and buffeting noise [D]. Doctoral Thesis, Changsha, China: Hunan University, 2011(in Chinese).
- [5] Yin S., Gu Z., Zong Y. et al. Sound quality evaluation of automobile side-window buffeting noise based on large-eddy simulation [J]. *Journal of Low Frequency Noise, Vibration and Active Control*, 2019, 38(2): 207-223.
- [6] Nelson P., Halliwell N., Doak P. Fluid dynamics of a flow excited resonance Part II: flow acoustic interaction [J]. *Journal of Sound and Vibration*, 1983, 91(3): 375-402.
- [7] Ota D., Chakravarthy S., Becher T. et al. Computational study of resonance suppression of open sunroofs [J]. *Journal of Experimental Psychology*, 1994, 116(4): 401-404.
- [8] Mendonca F. CFD/CAE combinations in open cavity noise predictions for real vehicle sunroof buffeting [J]. *SAE International Journal of Passenger Cars-Mechanical Systems*, 2013, 6(1): 360-368.
- [9] Dunai L., Lengua I., Iglesias M. et al. Buffeting-noise evaluation in passenger vehicle BMV 530d [J]. *Acoustical Physics*, 2019, 65(5): 578-582.
- [10] Gu Z., Xiao Z., Mo Z. Review of CFD simulation on vehicle wind buffeting [J]. *Noise and Vibration Control*, 2007, 27(4): 65 -68.
- [11] Wang Y. P., Gu Z. Q., Yang X. et al. Numerical simulation and control of automobile sunroof buffeting noise [J]. *China Journal of Highway and Transport*, 2010, 23(6): 108-114.
- [12] Wang Y. P., Gu Z. Q., Yang X. Research and control of wind vibration characteristics of automobile side window [J]. *Acta Aerodynamica Sinica*, 2012, 30(3): 277-283.
- [13] Liu J., Yang D., Wang X. et al. Effect of turbulent boundary layer thickness on a three-dimensional cavity flow [J]. *Acta Aerodynamica et Astronautica Sinica*, 2016, 37(2): 475-483.
- [14] Liu C., Gao Y. S., Dong X. R. et al. Third generation of vortex identification methods: Omega and Liutex/Rortex based systems [J]. *Journal of Hydrodynamics*, 2019, 31(2): 205-223.
- [15] Hunt J. C. R., Wray A. A., Moin P. Eddies, stream, and convergence zones in turbulent flows [R]. Proceedings of the Summer Program. Center for Turbulence Research Report CTR-S88, 1988, 193-208.
- [16] Jeong J., Hussain F. On the identification of a vortex [J]. *Journal of Fluid Mechanics*, 1995, 285: 69-94.
- [17] Liu C., Wang Y. Q., Yang Y. et al. New omega vortex identification method [J]. *Science China Physics, Mechanics and Astronomy*, 2016, 59(8): 684711.
- [18] Dong X. R., Wang Y. Q., Chen X. P. et al. Determination of epsilon for omega vortex identification method [J]. *Journal of Hydrodynamics*, 2018, 30(4): 541-548.
- [19] Liu J. M., Wang Y. Q., Gao Y. S. et al. Galilean invariance of omega vortex identification method [J]. *Journal of Hydrodynamics*, 2019, 31(2): 249-255.
- [20] Liu C., Gao Y., Tian S. et al. Rortex-A new vortex vector definition and vorticity tensor and vector decompositions [J]. *Physics of Fluids*, 2018, 30(3): 035103.
- [21] Gao Y., Liu C. Rortex and comparison with eigenvalue-based vortex identification criteria [J]. *Physics of Fluids*, 2018, 30(8): 085107.
- [22] Wang Y. Q., Gao Y. S., Liu J. M. et al. Explicit formula for the Liutex vector and physical meaning of vorticity based on the Liutex-Shear decomposition [J]. *Journal of Hydrodynamics*, 2019, 31(3): 464-474.
- [23] Wang Y., Gao Y., Liu C. Letter: Galilean invariance of Rortex [J]. *Physics of Fluids*, 2018, 30(11): 111701.
- [24] Gao Y. S., Liu J. M., Yu Y. et al. A Liutex based definition and identification of vortex core center lines [J]. *Journal of Hydrodynamics*, 2019, 31(3): 445-454.
- [25] Dong X. R., Cai X. S., Dong Y. et al. POD analysis on vortical structures in MVG wake by Liutex core line identification [J]. *Journal of Hydrodynamics*, 2020, 32(3): 497-509.
- [26] Charkrit S., Shrestha P., Liu C. Liutex core line and POD analysis on hairpin vortex formation in natural flow transition [J]. *Journal of Hydrodynamics*, 2020, 32(6): 1109-1121.
- [27] Dong X., Gao Y., Liu C. New normalized Rortex/Vortex identification method [J]. *Physics of Fluids*, 2019, 31(1): 011701.
- [28] Hao L. Numerical simulation and PIV experimental research over a backward-facing step and a square cylinder [D]. Master Thesis, Harbin, China: Harbin Institute of Technology, 2012(in Chinese).
- [29] Vogel J. C., Eaton J. K. Combined heat transfer and fluid dynamic measurements downstream of a backward-facing step [J]. *Journal of Heat Transfer*, 1985, 107(4): 922-929.
- [30] Wu J., Ning F. Hybrid RANS-LES method applied to backward-facing step flow [J]. *Journal of Beijing University of Aeronautics and Astronautics*, 2011, 37(6): 701-704(in Chinese).
- [31] Zang Y. Numerical simulation of vehicle aerodynamics [M]. Beijing, China: Peking University Press, 2011(in Chinese).